PHYSICAL REVIEW A VOLUME 41, NUMBER 5 1 MARCH 1990

# Intermittency and chaos in intracavity doubled lasers. II

Glenn E. James and Evans M. Harrell II
*School of Mathematics, Georgia Institute of Technology, Atlanta, Georgia 30332*

Rajarshi Roy
*School of Physics, Georgia Institute of Technology, Atlanta, Georgia 30332*

(Received 23 June 1989)

We describe the nonlinear dynamics of intracavity doubled multimode lasers. Baer [J. Opt. Soc. Am. B **3**, 1175 (1986)] observed irregular amplitude fluctuations in a multimode yttrium aluminum garnet laser with an intracavity potassium titanyl phosphate frequency-doubling crystal; we identify type-III intermittency as the route to chaos. Subsequently, Oka and Kubota [Opt. Lett. **13**, 805 (1988)] demonstrated the stabilization of such a laser by the introduction of a quarter wave plate into the cavity. A generalized model of rate equations for this case is introduced. It is shown that a second route to chaos through a Hopf bifurcation, synchronization, and period-doubling sequence occurs on rotation of the quarter wave plate within the cavity. In addition, we predict that the laser output may be stable for particular lengths of the doubling crystal.

## I. INTRODUCTION

The development of novel solid-state laser materials has resulted in compact, narrow linewidth sources of radiation in the near-infrared region. Furthermore, through intracavity frequency doubling of these lasers, it is possible to generate light in the visible range. Such lasers and their doubled counterparts have been used for injection-seeding high-power lasers and will in the future replace more delicate, difficult to maintain gas lasers in many applications.[1]

Our emphasis in this paper will be on fundamental nonlinear dynamical phenomena like those that have been experimentally observed in intracavity double yttrium aluminum garnet (YAG) laser by Baer.[2] With a frequency-doubling crystal in the cavity, Baer noted large amplitude fluctuations in the output intensity during multimode operation. Kennedy and Barry carried out the stability analysis for such a laser operating with a single longitudinal mode.[3] The steady-state solutions of the multimode rate equations used by Baer, and their stability characteristics, have been analyzed thoroughly by Wu and Mandel.[4,5] Until now, there has been no comprehensive analysis of the global nonlinear dynamics which underlie the observed multimode instabilities. Such an analysis is motivated not only by the desire to stabilize intracavity doubled lasers; it also provides an important illustration of the rich and complex phenomenology associated with relatively simple nonlinear experimental systems. Predictions that are made in the course of this analysis will allow the validity of the basic models to be tested experimentally.

We will use numerical integration to examine the precise nature of the instability that was observed in an intracavity doubled YAG laser and the experimental resolution of this difficulty by Oka and Kubota.[6] We generalize the model of laser rate equations[2] to include arbitrary angular settings of a quarter wave plate (QWP) within the cavity. The dynamical behavior described by these new equations is then studied. Two different routes to chaos are established, one through intermittency and the other through a Hopf bifurcation and period doubling.

This paper is organized as follows. The basic rate equations for multimode intracavity doubled lasers are given in Sec. II. The modification of these equations when a QWP is inserted in the cavity is then dealt with for arbitrary settings of the plate's fast axis. The chaotic dynamics of the laser without the QWP is studied in Sec. III. We examine the route to chaos as the cross saturation parameters for the modes are varied, and discover intermittency. A quite different approach to chaos is obtained when we vary the setting of the QWP for a fixed value of the cross saturation parameters, as seen in Sec. IV. A Hopf bifurcation, synchronization, and period doubling are observed as the laser proceeds towards chaotic behavior. We conclude with a summary of our results and suggestions for future experiments. This paper expands upon a previous work.[7]

## II. MODELS FOR INTRACAVITY-DOUBLED LASERS

The laser system we use to exemplify intracavity doubling is the diode-pumped YAG laser with an intracavity potassium titanyl phosphate (KTP) crystal shown in Fig. 1. The left end of the YAG rod is coated to transmit the diode laser radiation, and reflect the YAG fundamental wavelength (1.06 $\mu$m) and second harmonic wavelength (0.532 $\mu$m) with high efficiency. The KTP crystal is type-II phase matched. The output mirror transmits the green, but is a high reflector for the fundamental wavelength. It is possible to select a small number of lasing modes by introducing etalons into the cavity.

Without a quarter wave plate in the cavity, Baer observed large, irregular amplitude fluctuations of the total

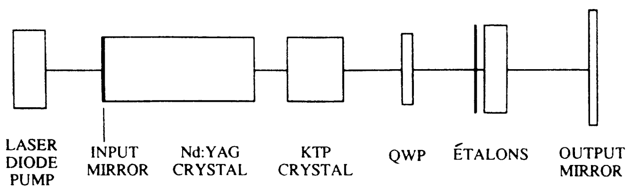

FIG. 1. Schematic of the diode-pumped YAG laser with intracavity KTP doubling crystal. Baer's laser used no QWP. Oka and Kubota included the QWP but did not restrict the number of longitudinal modes with étalons.

intensity of the second harmonic when the laser was operated in three or more longitudinal modes.[2] In two mode operation, periodic pulsations were observed. To utilize the larger power output available in multimode operation, it is often necessary to eliminate the irregular fluctuations. Oka and Kubota did just this; they devised a scheme with an intracavity quarter wave plate that decoupled the field components along the fast and slow axes of the birefringent KTP crystal.[6] Stable multimode operation of the laser was obtained with the fast axis of the quarter wave plate aligned at $\pi/4$ radians with respect to the extraordinary axis of the KTP crystal.

Solid-state lasers like the Nd:YAG fall into the category of class-*B* lasers defined by Arecchi *et al.*[8] Also included in this class are Ti:sapphire and semiconductor lasers. For all class-*B* lasers, the relevant equations of motion are those for the intensity $I$ and the population inversion $G$; the polarization is adiabatically eliminated. The rate equations used by Baer to model $N$ longitudinal modes in an intracavity doubled laser were[2]

$$\tau_c \frac{dI_j}{dt} = \left[ G_j - \alpha_j - \epsilon I_j - 2\epsilon \sum_{\substack{k=1\\ k\neq j}}^{N} I_k \right] I_j \,, \qquad (2.1\text{a})$$

$$\tau_f \frac{dG_j}{dt} = G_j^0 - G_j \left[ 1 + \beta_j I_j + \sum_{\substack{k=1\\ k\neq j}}^{N} \beta_{jk} I_k \right] , \qquad (2.1\text{b})$$

where $j = 1, 2, \ldots, N$; $\tau_c$ and $\tau_f$ are the cavity round trip time and fluorescence time, respectively; $\alpha_j$ is the cavity loss for the $j$th mode; $G_j^0$ is the small signal gain; $\beta_j$ and $\beta_{jk}$ are self-saturation and cross saturation parameters; and $\epsilon$ is the nonlinear coupling coefficient due to the presence of the intracavity doubling crystal. In Eq. (2.1a), the quadratic terms $I_j^2$ and $I_j I_k$ account for the loss in intensity of the fundamental frequencies through second-harmonic generation and sum-frequency generation. Whereas in the first process two photons from the same longitudinal mode are converted into a green photon, the combination of photons from two different modes produces the sum frequency described by the intensity cross products. Baer identified this sum-frequency coupling as the nonlinearity which destabilizes Eqs. (2.1).

For a multimode laser modeled by these equations, the total intracavity intensity at the fundamental wavelength is expressed as the sum $I_1 + I_2 + I_3 + \cdots$. On the other hand, the total intracavity intensity at the second-harmonic wavelength is the combined effect of frequency-doubling and sum-frequency generation. The intensity of this signal is then

$$\epsilon \left[ \sum_{j=1}^{N} I_j^2 + 4 \sum_{\substack{j,k\\ j=1\\ j\neq k}}^{N} I_j I_k \right] . \qquad (2.2)$$

This distinction is important in order to compare the model with experiments, in which either the total fundamental or second-harmonic intensity is easily measured.

When a quarter wave plate is introduced into the laser cavity, its orientation is defined by the angle $\psi$ between the extraordinary axis of the birefringent KTP crystal and the fast axis of the QWP (Fig. 2). The birefringence of the QWP can split each longitudinal mode into two frequency components with different polarizations. Oka and Kubota examined the special cases when $\psi = \pi/4$ and when $\psi = 0$ or $\pi/2$. For the latter settings, they showed that the polarization modes were coupled through sum-frequency generation. At $\psi = \pi/4$, however, there was no sum-frequency generation; the intensities of the polarization modes were thus uncoupled, and the second-harmonic output was stabilized.

The analysis performed by Oka and Kubota began with the computation of the round-trip Jones matrix for the cavity configuration in Fig. 1, with no restrictions on the number of longitudinal modes.[6] We extend their analysis to include arbitrary values of the QWP angle $\psi$. Let $\delta = (n_e - n_0)(2\pi/\lambda) l$ be the single-pass birefringent phase shift of the fundamental wave (of wavelength $\lambda$) in the KTP crystal of length $l$; $n_o$ and $n_e$ are the refractive indices along the ordinary and extraordinary axes of the crystal. The Jones matrix can be determined from

$$M = C(\delta) R(\psi) C(\pi/2) C(\pi/2) R(-\psi) C(\delta) \,, \qquad (2.3)$$

where $C(\delta)$ is the matrix for the KTP birefringence, $R(\psi)$ is the QWP rotation, and $C(\pi/2)$ is the QWP retardation. The expanded round-trip matrix is then

$$M = i \begin{bmatrix} \exp(i\delta)\cos(2\psi) & \sin(2\psi) \\ \sin(2\psi) & -\exp(-i\delta)\cos(2\psi) \end{bmatrix} . \qquad (2.4)$$

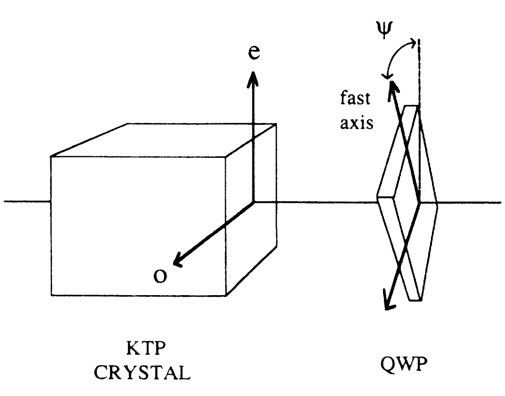

FIG. 2. The angle $\psi$ is defined by the relative position of the KTP crystal extraordinary axis and the fast axis of the QWP.

An electric field oscillating in a cavity described by the matrix $M$ must be an eigenvector of that matrix. Two general polarization states $\mathbf{E}_1(\omega_1)$ and $\mathbf{E}_2(\omega_2)$ with components along the extraordinary and ordinary axes of the KTP crystal can be defined as

$$\mathbf{E}_1(\omega_1)=(|E_1|/N_1)\exp[i(\omega_1 t+\varphi_1)]\begin{bmatrix}B_1\\ C_1\end{bmatrix} \tag{2.5a}$$

and

$$\mathbf{E}_2(\omega_2)=(|E_2|/N_2)\exp[i(\omega_2 t+\varphi_2)]\begin{bmatrix}B_2\\ C_2\end{bmatrix}, \tag{2.5b}$$

where $\varphi_1$ and $\varphi_2$ are arbitrary phase shifts and

$$\begin{aligned}&B_1=\cos(2\psi)\cos\delta+[\cos^2(2\psi)\cos^2\delta+\sin^2(2\psi)]^{1/2}\ ,\\ &C_1=\sin2\psi\ ,\\ &B_2=\{\cos(2\psi)\cos\delta\\ &\qquad-[\cos^2(2\psi)\cos^2\delta+\sin^2(2\psi)]^{1/2}\}/\sin2\psi\ ,\\ &C_2=1\ ,\\ &N_1=(B_1^2+C_1^2)^{1/2}\ ,\\ &N_2=(B_2^2+C_2^2)^{1/2}\ .\end{aligned} \tag{2.6}$$

These normalizations were chosen so that $\mathbf{E}_1$ and $\mathbf{E}_2$ are still orthonormal in the limit as $\psi\rightarrow0$ or $\pi/2$. The frequencies $\omega_1$ and $\omega_2$ are generally very close but not identical, so the sum frequency $(\omega_1+\omega_2)$ is very near $2\omega_1$. It is possible, in fact, that $\mathbf{E}_1$ and $\mathbf{E}_2$ are generated by the same longitudinal mode, due to the optical path difference through the QWP fast and slow axes. In that case, $\omega_1$ and $\omega_2$ are spaced by half of the cavity resonant spacing since the optical path length for the two polarizations differs by half a wavelength.

Now the polarization $P$ introduced by $\mathbf{E}_1(\omega_1)$ and $\mathbf{E}_2(\omega_2)$ can be calculated.[9] Let $E_o$ be the sum of the ordinary components of $\mathbf{E}_1$ and $\mathbf{E}_2$, and let $E_e$ be the sum of their extraordinary components. Then

$$\begin{aligned}P(\omega_1+\omega_2)&=d_{\rm eff}E_o(\omega_1,\omega_2)E_e(\omega_1,\omega_2)\\ &=d_{\rm eff}\left[\frac{E_1B_1}{N_1}e^{i(\omega_1t+\varphi_1)}+\frac{E_2B_2}{N_2}e^{i(\omega_2t+\varphi_2)}\right]\left[\frac{E_1C_1}{N_1}e^{i(\omega_1t+\varphi_1)}+\frac{E_2C_2}{N_2}e^{i(\omega_2t+\varphi_2)}\right],\end{aligned} \tag{2.7}$$

where $d_{\rm eff}$ is the effective nonlinear coefficient for KTP.

In this general setting, we can now work out the time-averaged second-harmonic output:

$$\begin{aligned}I(\omega_1+\omega_2)&=\langle P(\omega_1+\omega_2)P^*(\omega_1+\omega_2)\rangle\\ &=d_{\rm eff}^2\{I_1^2(B_1^2C_1^2/N_1^4)+I_2^2(B_2^2C_2^2/N_2^4)\\ &\qquad+I_1I_2[(B_1C_2+B_2C_1)^2/N_1^2N_2^2]\}\ .\end{aligned} \tag{2.8}$$

The $I_1^2$ and $I_2^2$ terms represent second-harmonic generation by the frequency doubling of each mode. The $I_1I_2$ cross term corresponds to sum-frequency generation. It is interesting to determine the relative weights of the coefficients in Eq. (2.8). First, a careful reduction shows that the coefficients for $I_1^2$ and $I_2^2$ are identical. We then define a doubling coefficient $g$ and a sum-frequency coefficient $\sigma$ by

$$g=4B_1^2C_1^2/(N_1^4)\ , \tag{2.9a}$$

$$\sigma=2(B_1C_2+B_2C_1)^2/(N_1^2N_2^2)\ . \tag{2.9b}$$

A straightforward calculation reveals the simple relation

$$\sigma=2(1-g)\ , \tag{2.10}$$

so that Eq. (2.8) finally becomes

$$I(\omega_1+\omega_2)=(d_{\rm eff}^2/4)[g(I_1^2+I_2^2)+4(1-g)I_1I_2]\ . \tag{2.11}$$

In the limits where $\psi=0$ and $\pi/2$, one finds $g=0$ and the green light is generated by sum-frequency generation. For the case where $\psi=\pi/4$, $g=1$ and only frequency doubling generates the second harmonic. These values, of course, precisely reproduce the calculations of Oka and Kubota:[6]

$$I(\omega_1+\omega_2)=\begin{cases}d_{\rm eff}^2I_1I_2, & \psi=0 \text{ or } \pi/2\\ (d_{\rm eff}^2/4)(I_1^2+I_2^2), & \psi=\pi/4\ .\end{cases} \tag{2.12}$$

Varying the QWP angle $\psi$ between these values causes a trade-off between the frequency-doubling losses and sum-frequency losses. In Fig. 3 we plot the coefficients $g$ and $\sigma$ as functions of the QWP setting $\psi$ and the KTP birefringence $\delta$. The curves are symmetric about $\psi=\pi/4$, and the values of $g$ and $\sigma$ at $\psi=0$, $\pi/4$, and $\pi/2$ are generally independent of the coefficient $\delta$. However, when $\delta=\pi/2$, Eqs. (2.9) indicate that $g$ is identically 1 and $\sigma$ is identically 0 for all values of $\psi$. This fact has important implications which will be discussed in Sec. IV.

The rate equations for a general setting of the quarter wave plate are now written ($j=1,2,\ldots,N$) as

$$\tau_c\frac{dI_j}{dt}=\left[G_j-\alpha_j-g\epsilon I_j-2(1-g)\epsilon\sum_{\substack{k=1\\k\neq j}}^{N}I_k\right]I_j\ , \tag{2.13a}$$

$$\tau_f\frac{dG_j}{dt}=G_j^0-G_j\left[1+\beta_jI_j+\sum_{\substack{k=1\\k\neq j}}^{N}\beta_{jk}I_k\right]\ . \tag{2.13b}$$

Only the coefficient $g$ contains the dependence on the angle $\psi$ between the QWP fast axis and the KTP crystal ex-

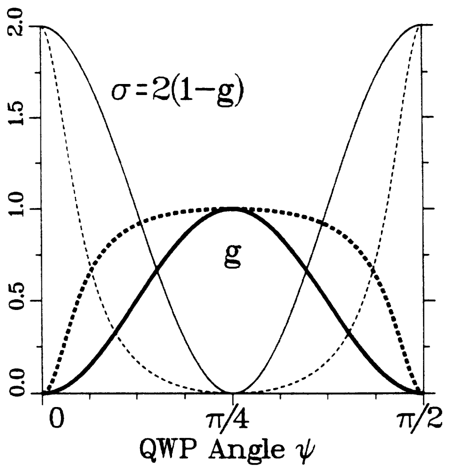

FIG. 3. The doubling coefficient $g$ (thick lines) and sum frequency coefficient $\sigma$ (thin lines) are functions of the QWP angle $\psi$ and the KTP birefringence $\delta$ (——, $\delta=0$ and $\pi$; — — —, $\delta=0.4\pi$ and $0.6\pi$).

traordinary axis. In these equations it is assumed that the losses due to sum-frequency generation are divided equally between the participating modes. Thus, the cross term coefficient in (2.13a) is $2(1-g)$, not $4(1-g)$ as in Eq. (2.11). The coefficient $\epsilon$ (in units of $\text{W}^{-1}$) can be obtained from the coefficient $d_{\text{eff}}$ (in units of m/V) by appropriate scaling:

$$\epsilon=d_{\text{eff}}^2/(4\epsilon_0 cD^2) , \tag{2.14}$$

where $D$ is a suitable atomic length parameter for the crystal. The gain equation, Eq. (2.13b), is unaffected by the presence of the QWP.

We note a subtlety in the definition of the $I_j$ variables in equation (2.13a). In the previous model [Eqs. (2.1)] $I_j$ represented the intensity of a longitudinal mode at a given frequency. With a QWP in the cavity, each longitudinal mode is split into two polarization modes of different frequencies. This is due to the optical path difference through the fast and slow axes of the QWP. Thus, for a laser cavity which allows $M$ longitudinal modes to oscillate, there can be up to $2M$ different frequency components $\mathbf{E}_j(\omega_j)$ present in the cavity. The variables $I_j$ then represent the intensities of these frequency components.

In Eq. (2.13a), the magnitudes of the losses due to frequency-doubling and sum-frequency generation depend on the value of $g$, which varies continuously with the QWP setting $\psi$. It should thus be experimentally straightforward to study the dynamics of the laser as the angle $\psi$ is changed. In the following sections we will determine the characteristics of the chaotic dynamics predicted by the model equations (2.1) and Eqs. (2.13).

## III. INTERMITTENCY ROUTE TO CHAOS

The model equations (2.1a) and (2.1b) are a set of coupled differential equations with quadratic nonlinearities which describe second-harmonic generation in a class-$B$ laser. The example from which we draw parameter values for our calculations is the intracavity doubled YAG laser operating with multiple longitudinal modes.

The large irregular amplitude fluctuations noticed by Baer in such a laser are clearly deterministic in origin. It is important to note that the time scales for decay of the fundamental intensity $[(\tau_c/\alpha_j)\approx 30$ nsec] and for the gain ($\tau_f=0.24$ msec) are rather different in magnitude in a YAG laser. The intensities of the modes are thus determined almost instantaneously by the values of the gain variables. Therefore, it is not surprising that three or more modes must exist in the laser before chaotic behavior arises.

The magnitudes of the cross saturation parameters $\beta_{jk}$ determine the extent of coupling between the different modes in the laser. If these are very small ($\beta_{jk}\approx 0$), the modes are essentially independent of each other, and there is no competition between them. They may then all coexist in steady-state operation. This situation can occur if the gain medium is inhomogeneously broadened and if there is little spatial overlap of the modes. If the coupling between the modes is appreciable, i.e., spatial hole burning is not a major factor, and the gain medium is primarily homogeneously broadened, the parameters $\beta_{jk}$ may be sizeable. Baer took $\beta_{jk}=0.66$ in his calculations and obtained irregular amplitude fluctuations. It is possible to vary the coupling between the modes by changing the cavity configuration and étalon characteristics. In the calculations reported here, we examine the behavior of the laser as the magnitude of the cross saturation coefficients is changed.

To simplify the model and computations, we limited the laser to three active modes which are sufficient to allow interesting chaotic dynamics to occur. The behavior of the total intensity $(I_1+I_2+I_3)$ then displays the experimentally observed irregular fluctuations. The basic dynamics are also unaffected by the choice of symmetric mode parameters in Eqs. (2.1):

$$\begin{gathered} \alpha_j=\alpha , \\ G_j^0=\gamma , \\ \beta_{jk}=\beta,\quad j,k=1,2,3 . \end{gathered} \tag{3.1}$$

We have scaled the intensity so as to let $I_j$, $\beta$, and $\epsilon$ be dimensionless, and to let $\beta_j\equiv 1$. The gains $G_j$ are already dimensionless. The other parameter values used by Baer[2] were $\tau_c=0.5$ nsec, $\tau_f=0.24$ msec, $\alpha=0.015$, $\gamma=0.12$, and $\epsilon=5.0\times 10^{-5}$.

With these parameter settings, and $0<\beta<0.2910$, periodic behavior of the total intensity is observed. The individual mode intensities cycle on and off as shown in Fig. 4(a); we call this cycle of alternating peak intensities, $I_1$-$I_2$-$I_3$-$I_1$- $\cdots$ , a forward sequence. This periodic solution coexists in phase space with an analogous reverse sequence whose intensity peaks alternate in the reverse order, $I_3$-$I_2$-$I_1$-$I_3$- $\cdots$ . For these values of $\beta$, the two sequences appear to be the only stable solutions; initial conditions dictate which solution is selected.

In Fig. 4(a) we note that when $I_1$ turns on and peaks, the other two intensities are negligible. In fact mode 1 behaves there as if the other modes were not oscillating at all. This suggests that we may look for some lower dimensional behavior in our six variable system of differential equations. We find that the important dynamical information, i.e., the signal for when the $j$th mode turns on, lies in the individual gain equations. Thus it is in the portion of phase space defined by $G_1$, $G_2$, and $G_3$ where we look for evidence of the route to chaos.

We define the Poincaré map $M$ on the transversal surface $G_1=0.017$ where points in the flow have the coordinate $G_1=0.017$ and $(dG_1/dt)<0$. For a point $\mathbf{x}$ on this surface, $M\mathbf{x}$ is defined by numerical integration of the flow until the next time that $G_1=0.017$ and $G_1$ is decreasing as the flow passes through the surface. $M$ maps a five component vector $(I_1,I_2,G_2,I_3,G_3)$ to another five component vector. However, the relevant dynamics can be seen in the $G_2$-$G_3$ plane. This projection of the Poincaré map is pictured in Fig. 5.

The plot in Fig. 5(a) is for 1200 iterations of $M$ when $\beta=0.2910$. First, we notice the structure of the two $S$-shaped curves, symmetric across the line $G_2=G_3$. Each periodic solution appears in the Poincaré map as a fixed point, so each curve highlights the stable and unstable manifolds of those fixed points. The form of the Eqs. (2.1) requires symmetry in the flow on either side of $G_2=G_3$, so all the structure above the line must be mirrored in the flow below the line. The result of reflecting all the points in Fig. 5(a) to the region below $G_2=G_3$ appears in Fig. 5(b). In this way, the 1200 points can be utilized to give twice the resolution of the map.

We examine the "flow" of these Poincaré maps more closely in Fig. 6(a). The fixed point that represents the reverse sequence has been reflected onto the point that represents the forward sequence. This point $C$ corresponds to a stable periodic orbit in phase space. For

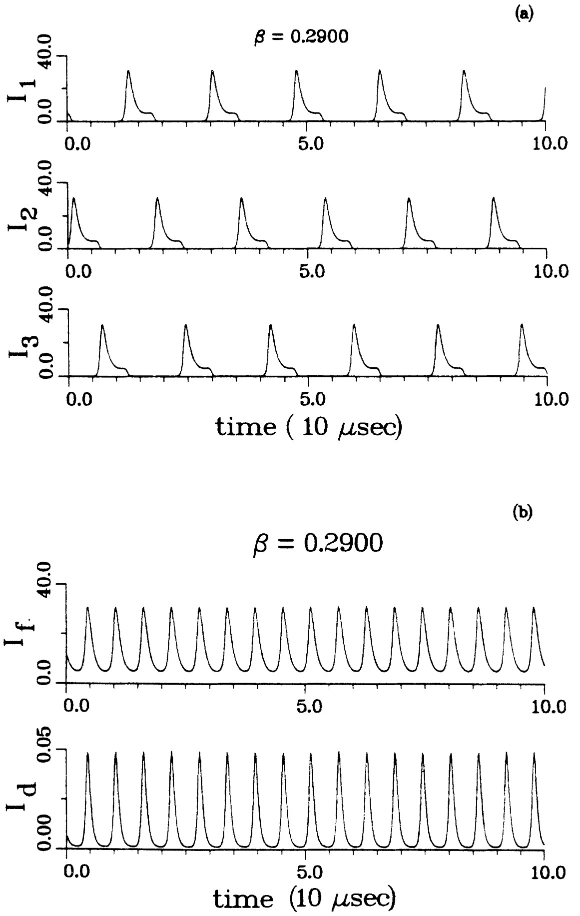

FIG. 4. (a) Periodic output of the individual intensities (in arbitrary units) for the cross saturation term $\beta=0.2900$. The regular pattern of intensity peaks makes a forward sequence. (b) The total fundamental intensity $I_f$ $(I_1+I_2+I_3)$ and total second-harmonic intensity $I_d$ [Eq. (2.2)] corresponding to the output in Fig. 4(a). Intensities are plotted in arbitrary units.

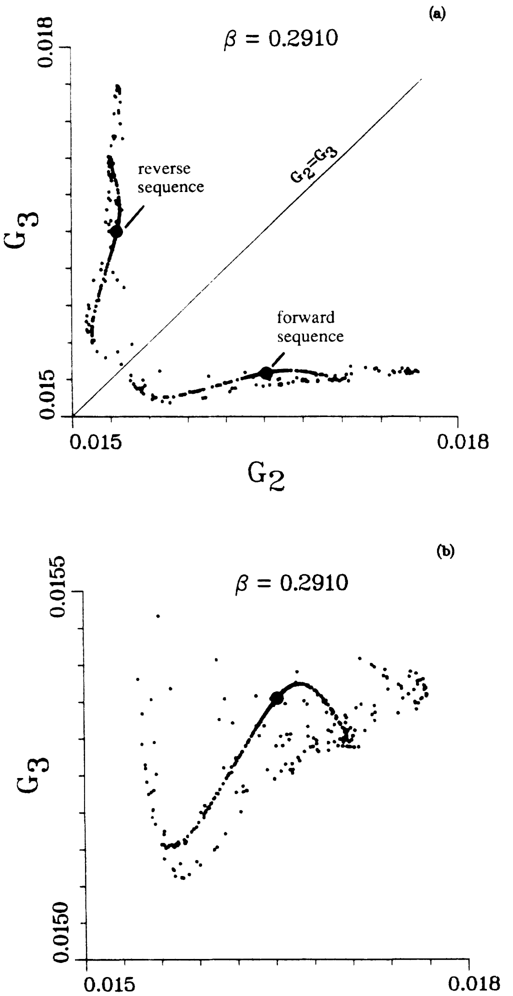

FIG. 5. (a) With $\beta=0.2910$, 1200 points of the Poincaré map $M$ for a single trajectory on the plane $G_1=0.017$. The points which correspond to the forward and reverse sequences represent periodic orbits in the full phase space. $G_j$ is the dimensionless gain for the $j$th mode $(j=1,2,3)$. (b) The same 1200 points as Fig. 5(a), reflected below the line $G_2=G_3$.

$0<\beta<0.2910$, the numerical trajectories were attracted to one of the periodic sequences for all the initial conditions that were attempted.

We can deduce important qualitative features of the flow dynamics from several simple observations of how $M$ maps the points on the curve which passes through $C$. First, points on the curve to one side of $C$ are mapped to the opposite side of $C$. The point $S_1$, for instance, is mapped to $S_2$. This indicates the existence of a Floquet multiplier (of the Jacobian of $M$ evaluated at $C$) with a negative real part. Such a multiplier will eventually signal the type of intermittency in the system. Next, all the points on the curve between $S_1$ and $S_2$ are mapped toward $C$, as indicated by the arrows. (This is a map, not a continuous flow, so the arrows indicate only tendencies of the map.) The negative multiplier still causes points to flip-flop across $C$, but along this arc they converge towards $C$ with each iteration. Finally, the points outside the $S_1$-$S_2$ arc are repelled from $S_1$ and $S_2$ until they leave the curve. After falling off the curve, a point will be

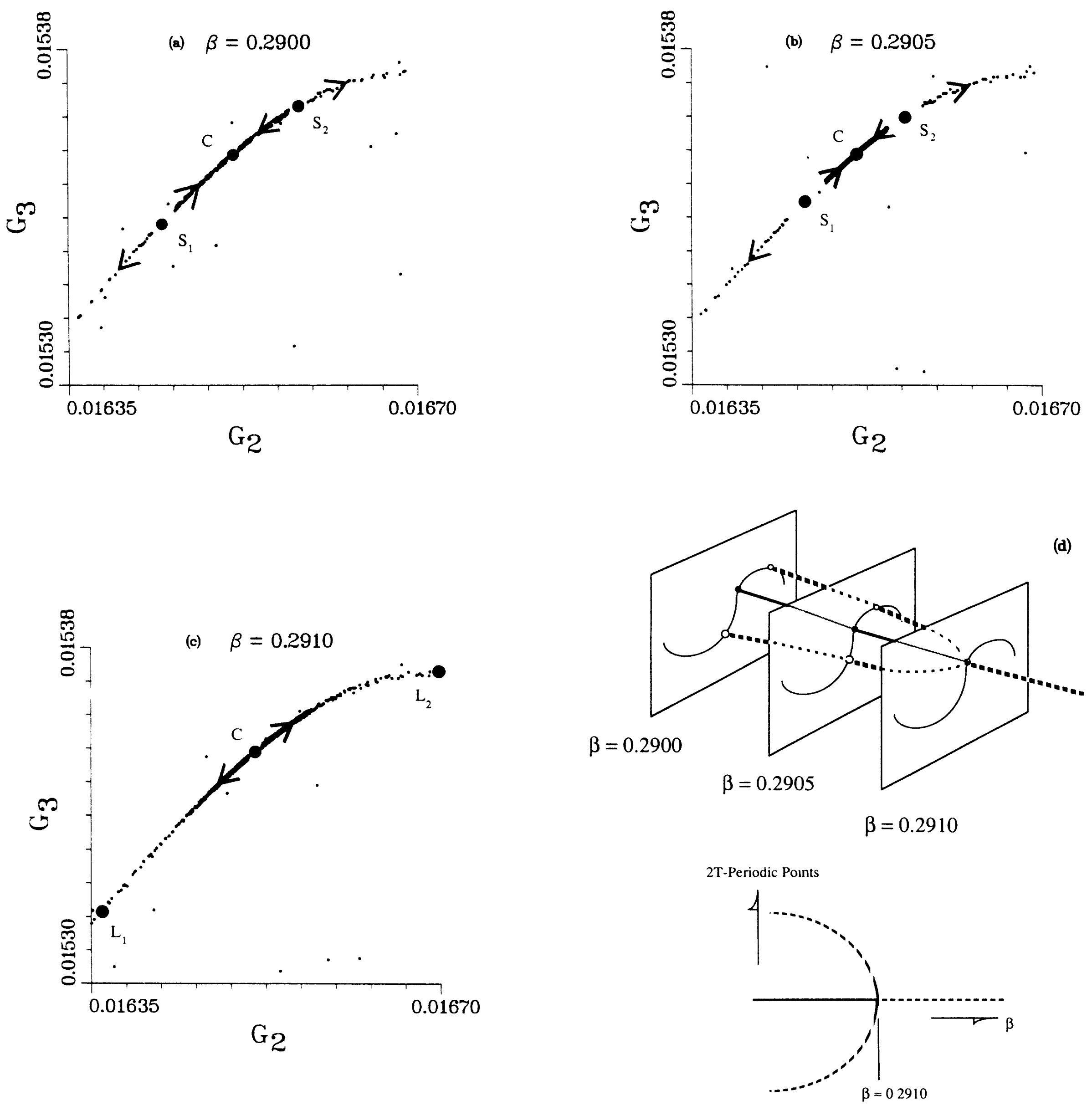

FIG. 6. (a) The reflected Poincaré map for $\beta=0.2900$. The stable point $C$ corresponds to a $T$-periodic solution. The saddle points $S_1$ and $S_2$ correspond to an unstable $2T$-periodic solution. The map $M$ is not a continuous flow in the plane, so the arrows indicate only tendencies of the map. $G_2$ and $G_3$ are the dimensionless gains for the second and third modes, respectively. (b) The reflected Poincaré map for $\beta=0.2905$. (c) The reflected Poincaré map for $\beta=0.2910$. (d) Schematic of the inverse pitchfork bifurcation of $2T$-periodic points for $\beta$ near 0.2910. Solid lines indicate stable points; dashed indicate instability. We note that the $T$-periodic point $C$ is also $2T$-periodic.

mapped either towards the opposite fixed point or will return to a neighborhood of the $S_1$-$S_2$ arc.

The global dynamics in Fig. 6(a) with $\beta=0.2900$ are now more clear. The curve through $C$ is strongly attractive in the transverse direction. The point $C$ is a stable hyperbolic fixed point of $M$, and corresponds to a periodic solution of the flow, of some period $T$. The points $S_1$ and $S_2$ map onto each other under $M$, and correspond to an unstable periodic solution of period $2T$. There are regions of the phase space that allow passage from the vicinity of one periodic sequence to the other, but once a trajectory approaches the $S_1$-$S_2$ arc of one of the sequences, the trajectory will converge to that particular periodic orbit. In the unreflected $G_2$-$G_3$ plane we then have two stable $T$-periodic solutions and two unstable $2T$-periodic solutions.

In Fig. 6(b), with $\beta=0.2905$, the stable and unstable manifolds of $C$ retain the same structure. The point $C$ is completely stable, while $S_1$ and $S_2$ are saddle points in the plane. However, for this increased value of $\beta$, the unstable $2T$-periodic solution indicated by $S_1$ and $S_2$ lies closer to $C$. In Fig. 6(c), $\beta=0.2910$, and the points $S_1$ and $S_2$ have collapsed onto $C$ so that $C$ is transformed into a saddle in this plane. As $\beta$ increases through 0.2910 we get the inverse pitchfork bifurcation sketched in Fig. 6(d). The transfer of instability at the critical value ($\beta\approx0.2910$) renders the $T$-periodic solution unstable and provides the mechanism for intermittency.

The laminar or regular portion of the intermittent flow appears for points in the neighborhood of $C$ [Fig. 6(c)]. This point is still strongly attractive in the transverse direction. Moreover, the periodic orbit is just barely unstable for $\beta\approx0.3$, so points near $C$ are mapped away very slowly. This implies that initial conditions very close to $C$ may appear $T$ periodic (or even $2T$ periodic) for a long time. Such flow constitutes the laminar portion of the intermittent behavior.

Turbulent flow appears eventually because the instability of $C$ forces points away from it, and all trajectories must proceed off the end of the $L_1$-$L_2$ curve in Fig. 6(c). Once off the curve, a trajectory wanders about in a fairly thin attractor in the phase space until it approaches a neighborhood of either periodic sequence. The trajectory then reenters the laminar region of phase space. The typical time history in Fig. 7 clearly displays the laminar and turbulent behaviors in the total fundamental intensity.

To characterize the intermittency, we have already observed the inverse pitchfork bifurcation which suggests that the primary Floquet multiplier passes through $-1$. We confirm this analytically by calculating the eigenvalues of an approximation to the Jacobian of $M$ in the neighborhood of $C$. We denote the equilibrium $C$ as the vector $\mathbf{c}=(c_1,c_2,c_3,c_4,c_5)$ and the unit basis vectors as $\hat{\mathbf{e}}_i$, $i=1,2,3,4,5$. Next we define small displacement vectors $\mathbf{h}_i=h_i\hat{\mathbf{e}}_i$, where the scalar quantity $h_i=0.001c_i$. We then formulate a standard approximation to the Jacobian by

$$J(\mathbf{c})=\left[\frac{M(\mathbf{c})-M(\mathbf{c}-\mathbf{h}_1)}{h_1},\ldots,\frac{M(\mathbf{c})-M(\mathbf{c}-\mathbf{h}_5)}{h_5}\right]. \tag{3.2}$$

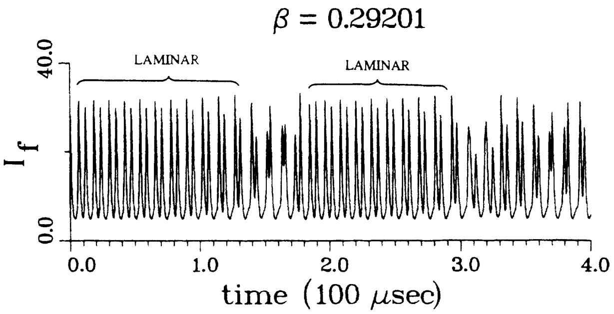

FIG. 7. For $\beta=0.29201$, the total fundamental intensity (in arbitrary units) displays regions of laminar and turbulent behavior.

This approximation requires $J$ to be nonsingular at $\mathbf{c}$, which is true except for $\beta$ precisely equal to its critical bifurcation value, slightly less than 0.2910.

It is straightforward to find the coordinates of $\mathbf{c}$ when $\beta<0.2910$, where $\mathbf{c}$ is stable. In such a case, one simply numerically integrates until the trajectory converges to a small neighborhood of the periodic orbit. However, for values of $\beta$ greater than 0.2910, $\mathbf{c}$ is unstable and one must find this point another way. We used the Poincaré map $M$ and defined a function $F(\mathbf{x})=\mathbf{x}-M(\mathbf{x})$. Even though $\mathbf{c}$ is unstable, it is still a zero of $F$, so we used a discrete Newton's method to find this zero. This technique for locating unstable fixed points of the Poincaré map is known as homotopic continuation.[10,11]

We calculated the eigenvalues of several approximations to $J$ for $\beta\approx0.3$ (Fig. 8). The periodic point loses its stability when $\beta\approx0.291$ and the principal eigenvalue of $J$ decreases through $-1$. This clearly characterizes the loss of stability as type-III intermittency.[12]

Further evidence of type-III behavior appears in the

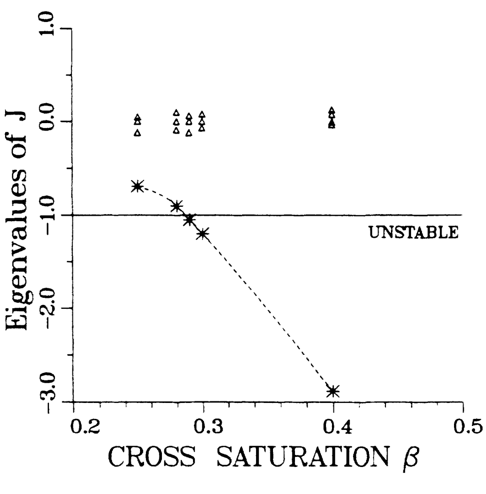

FIG. 8. Eigenvalues of the Jacobian $J$, evaluated at the equilibrium $C$, for $\beta=0.2500, 0.2800, 0.2900, 0.3000, 0.4000$ (dimensionless). All eigenvalues are real for $\beta$ in this range. $C$ becomes unstable when the magnitude of the principal eigenvalue (indicated by $*$) is greater than 1.

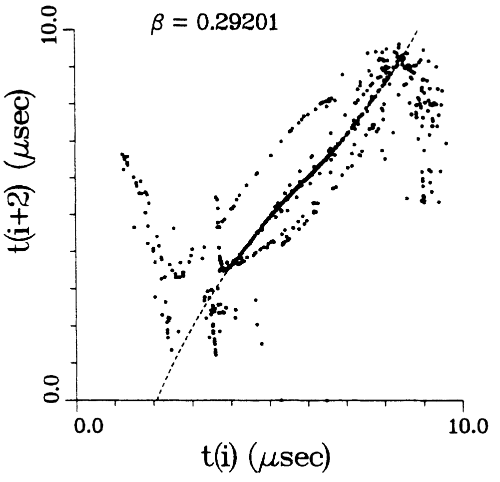

FIG. 9. For $\beta=0.29201$, 1000 consecutive peak-to-peak times $t(i)$ of the total fundamental intensity $(I_1+I_2+I_3)$. The plotted cubic is $0.03(t-5.9)^3+1.1(t-5.9)+5.9$.

time spacing between peaks in the total intensity. We begin with a long numerical trajectory for the example $\beta=0.29201$ (part of which is shown in Fig. 7) and create a sequence $\{t_1,t_2,t_3,\ldots\}$ of 1000 peak-to-peak times. In Fig. 9 we plot the second return times for this sequence, i.e., $t_{i+2}$ versus $t_i$. The resulting figure displays the locally cubic form which is typical of the generic return map that generates type-III intermittency.[13]

The type of intermittency is also evident in the distribution of the durations of laminar flow in a single trajectory. Pomeau and Manneville indicate the approximate distribution which is characteristic of this type of intermittency.[13] We defined laminar behavior in our numerical trajectory as flow whose intersection with the plane $G_1=0.17$ lies in the $L_1$-$L_2$ curve in Fig. 6(c). Since the time of return to the plane remains nearly constant for points near $C$, we approximated the duration of laminar flow by counting the number of consecutive points which stay on the curve. The distribution of this count in Fig. 10 conforms to the model distribution described by Pomeau and Manneville. The long tail in this histogram is weighted (in the limit) such that the distribution is not normalizable. A meaningful characteristic time scale, then, is an average of the inverse of the laminar flow duration. We found the period of the Poincaré map in the laminar region to be approximately 18 $\mu$sec. We then defined the time duration of laminar flow $t_l=(18\ \mu\text{sec})\times$(the number of consecutive points on $L_1$-$L_2$) and calculated $\langle 1/t_l\rangle \approx \frac{1}{70}\ \mu\text{sec}^{-1}$.

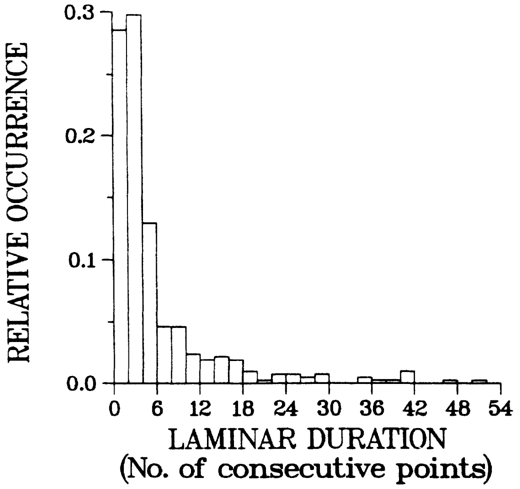

FIG. 10. The distribution of the duration of laminar behavior in a single trajectory for $\beta=0.29201$. The relative occurrence was calculated with respect to 410 laminar regions.

The transition from intermittency to "complete" chaos, for larger values of $\beta$, is difficult to detect numerically. The $L_1$-$L_2$ curve in Fig. 6(c) is an unstable manifold of $C$, and flow on that curve eventually returns to a neighborhood of $C$'s stable manifold. However, the thinness of the attractor around $L_1$-$L_2$ obscures the trajec-

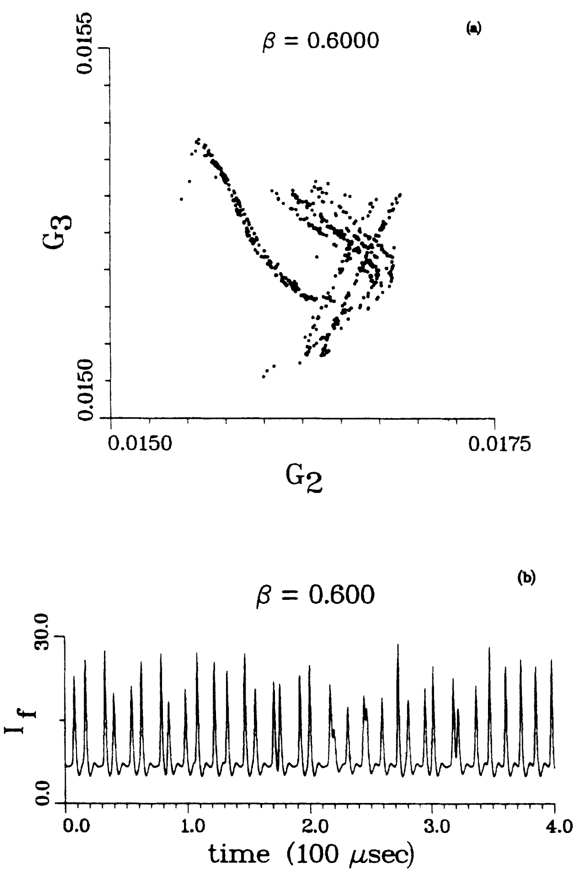

FIG. 11. (a) Chaotic flow on the Poincaré section $G_1=0.017$ for $\beta=0.6000$. $G_j$ is the dimensionless gain for the $j$th mode $(j=1,2,3)$. (b) Total fundamental intensity output (in arbitrary units) for $\beta=0.6000$.

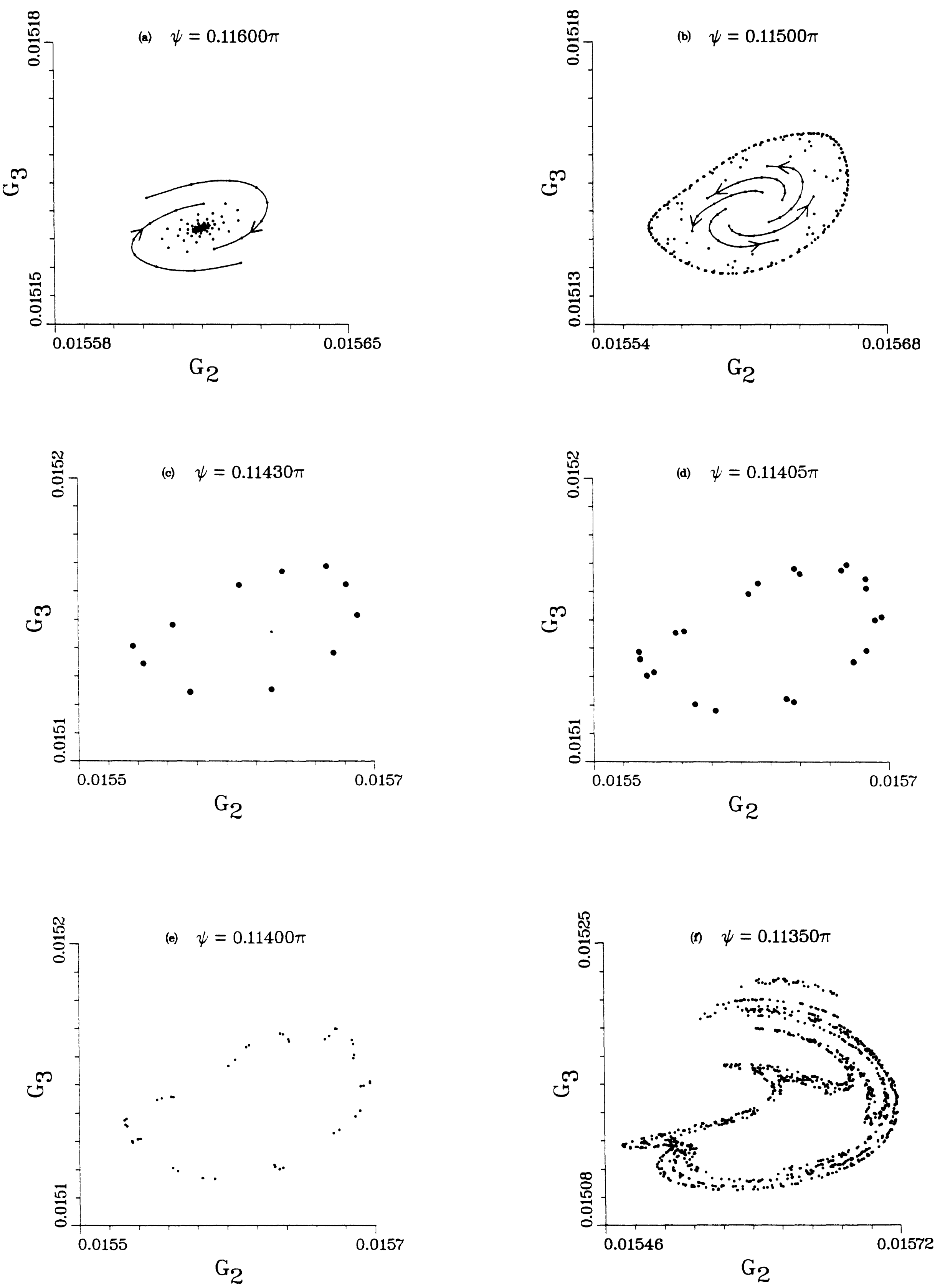

FIG. 12. (a)–(h) Poincaré maps for $\psi$ varying from $0.11\,600\pi$ to $0.11\,290\pi$. $G_2$ and $G_3$ are the dimensionless gains for the second and third modes, respectively.

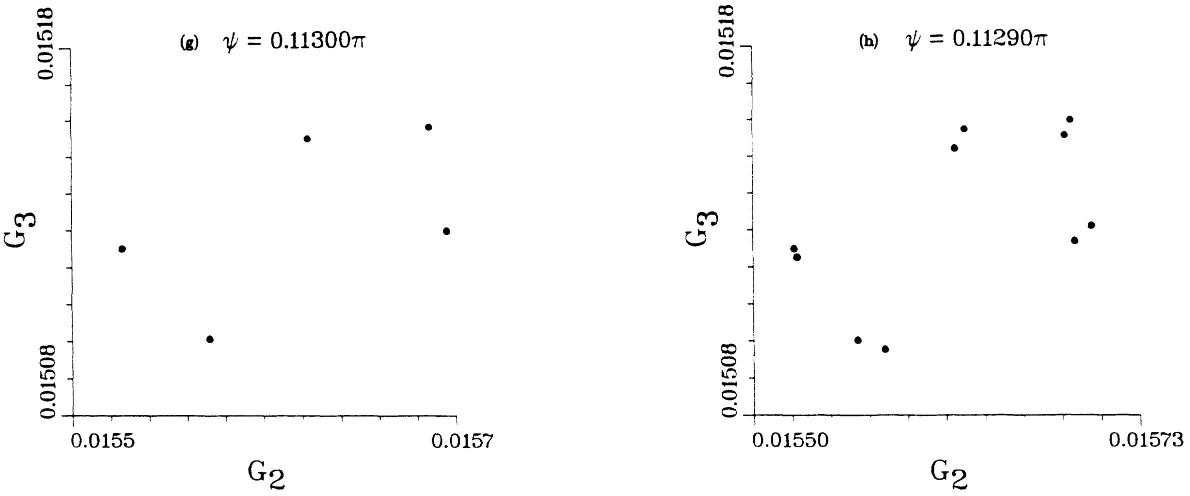

FIG. 12. (*Continued*).

tories returning to $C$. We conjecture that, at some value of $\beta$ between 0.4 and 0.6, the unstable manifold becomes tangent to the stable manifold. The complications in the flow contingent with the creation of such a tangency are sufficient to produce chaos.[14,15]

When $0.4<\beta<0.96$, the flow is chaotic on a strange attractor like the one shown in Fig. 11(a). The chaotic intensity output for $\beta=0.60$, the approximate experimental value used by Baer, is shown in Fig. 11(b). Another transition occurs for $\beta$ between 0.96 and 0.98. We observe an inverse cascade which stabilizes the flow, and for $\beta>0.98$ the only allowed solutions are those for which a single intensity is stable and nonzero, while the other two intensities are forced to zero. This behavior persists for values of $\beta$ up to 2.0.

As in the numerical studies of Shih *et al.*,[16] we have identified a particular route to chaos which has been observed in experiments. The Poincaré maps, in particular, allow us to trace the specific origins of the instability which generates type-III intermittency in this system. It is also interesting to note that the chaotic behavior appears via coupling in the intensity relations rather than in the complex field equations.

## IV. ROUTE TO CHAOS VIA QWP SETTING

In this section we study the chaotic dynamics of Eqs. (2.13) which model intracavity doubling with a quarter wave plate (QWP) in the cavity. A comparison of Eqs. (2.1) and (2.13) reveals that the entire effect of the quarter wave plate is contained in the parameter $g$, which depends on the birefringence of the doubling crystal, $\delta$, and the angle $\psi$ between the fast axis of the QWP and the extraordinary axis of the KTP crystal. There is a trade-off between the production of green light by frequency-doubling and sum-frequency generation. The factors of the quadratic terms in (2.13a) are such that when $g=1$ ($\psi=\pi/4$), only frequency doubling occurs, while when $g=0$ ($\psi=0$ or $\pi/2$), sum-frequency generation is the only mechanism for production of green light. Thus, the QWP setting enhances the role of one or the other source of nonlinearity in Eq. (2.13a).

Oka and Kubota have shown experimentally that the output intensity of the laser is stable when $g=1$, and irregular when $g=0$. A linear-stability analysis for the former case supports their experimental observation; in the latter case, a numerical study of the dynamics is necessary to obtain a full understanding of the system. We report in this section the results of an investigation of the dynamical behavior of the laser predicted by Eqs. (2.13) for different settings of the QWP, starting with the stable behavior at $\psi=\pi/4$, and progressing towards chaos as $\psi$ is decreased to 0. Exactly similar behavior would be seen if $\psi$ were increased to $\pi/2$ since $g$ is a symmetric function of $\psi$ (Fig. 3).

The steady-state stability of Eqs. (2.13) when $g=1$ is very important with respect to $g$'s dependence on the KTP birefringence $\delta$. It has already been shown that for $\delta=\pi/2$ the parameter $g$ is identically one. This implies that if one can produce a KTP crystal whose birefringence is an odd multiple of $\pi/2$, the model equations (2.13) predict the laser will have stable steady state output regardless of the QWP angle $\psi$.

We again limited our system of equations (2.13) to $N=3$, the minimum number of intensity and gain relations necessary to allow chaotic behavior. We also chose symmetric parameters as in Eqs. (3.1). We fixed the cross saturation parameter $\beta$ at 0.60, which was sufficient coupling in Eqs. (2.1) to allow the generation of chaos. We calculated the KTP birefringence $\delta$ using crystal length[6] $l=3.4$ mm and refractive indices[17] $n_e=1.7458$ and $n_o=1.7381$. The other parameter values were the same as in Sec. III: $\beta_j=1$ ($j=1,2,3$), $\tau_c=0.5$ nsec, $\tau_f=0.24$ msec, $\alpha=0.015$, $\gamma=0.12$, and $\epsilon=5.0\times10^{-5}$.

For $\psi=\pi/4$, where the intensity relations are uncoupled, we see a stable steady-state solution with all three intensities identical. This steady state persists until $\psi\approx0.1250\pi$, when two $T$-periodic solutions arise, a forward and reverse sequence like those seen in Sec. III. The fact that the steady state remains stable for such a large range of $\psi$ suggests that, for our selection of param-

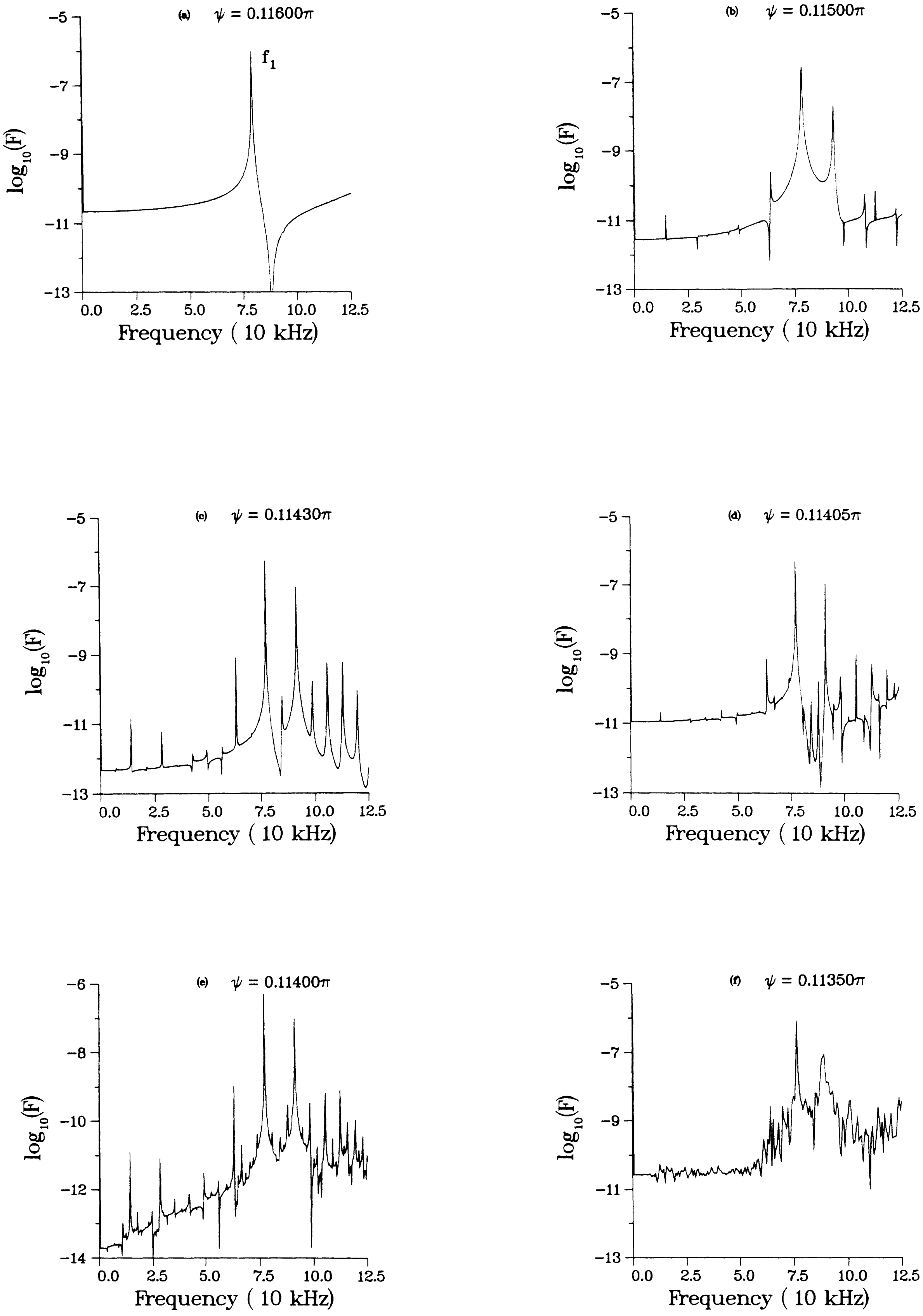

FIG. 13. (a)–(h) Power spectra $F$ of the total intensity output corresponding to the maps in Fig. 12.

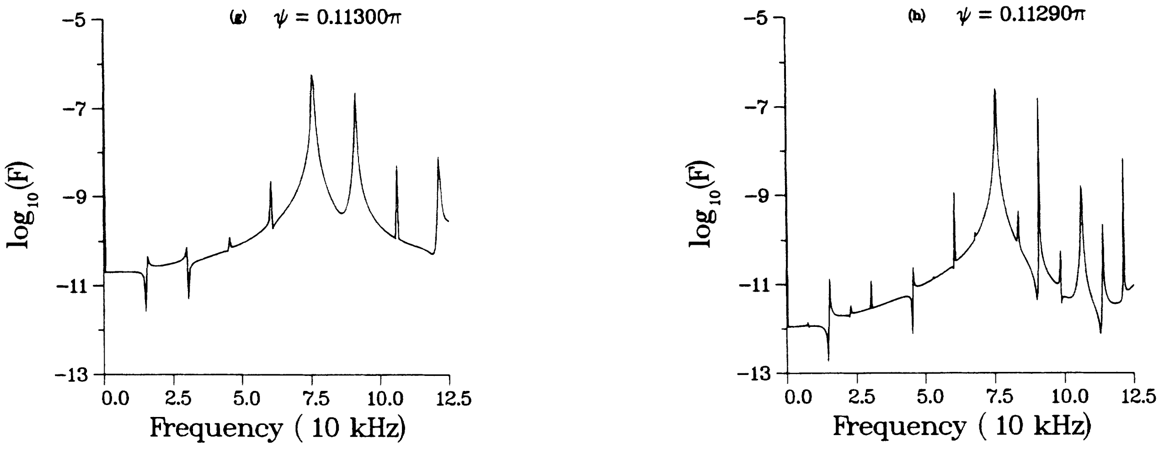

FIG. 13. (*Continued*).

eters, the laser output is not sensitive to the precision of the QWP setting near $\psi=\pi/4$. While $\psi$ is between $0.1250\pi$ and $0.1200\pi$, the stable steady state coexists in phase space with the two stable periodic sequences; initial conditions dictate which solution eventually attracts a trajectory. These three solutions all lose their stability when $\psi$ is less than $0.1200\pi$. At this same value of $\psi$, a period doubling occurs (from each periodic sequence) and produces a $2T$-periodic solution. The Poincaré map in the $G_2$-$G_3$ plane reveals the interesting flow structure in the neighborhood of this solution. In Fig. 12(a), the $2T$-periodic flow corresponds to the point at the center of the spirals; the two inward spirals are points which belong to a single trajectory. This suggests the presence of complex conjugate Floquet multipliers with negative real parts. The logarithm of the frequency spectrum $F$ shown in Fig. 13(a) is calcualted from the fast Fourier transform of the total fundamental intensity; $f_1$ is the frequency of the $2T$-periodic solution.

The next transition, for $\psi \approx 0.1150\pi$, is a Hopf bifurcation to a stable torus. In Fig. 12(b) a single trajectory spirals outward along five distinct spirals to a closed loop in the plane. This loop is the cross section of a stable torus in the full phase space. There are two main frequencies governing this trajectory. The first, $f_1$, corresponds to the trajectory's time of first return to the plane; this frequency is necessarily very close to that of the $2T$-periodic orbit. Some second frequency, $f_2$, corresponds to the time needed to wind transversely about the torus. For $\psi \approx 0.1150\pi$, $f_1/f_2$ is irrational, so the trajectory is dense on the torus and the Poincaré map shows a closed figure. When $\psi$ is further decreased to $0.1143\pi$, the frequencies synchronize to make $f_1/f_2$ rational, and the Poincaré section in Fig. 12(c) shows the 11 periodic points of a single trajectory. The route to chaos now follows a period-doubling sequence as $\psi$ takes on values from $0.1143\pi$ to $0.1135\pi$ [Figs. 12(c)–12(f)]. A typical intensity output in the chaotic regime is shown in Fig. 14. For $\psi < 0.1135\pi$ the flow is almost always chaotic [Fig. 12(f)], but there is at least one periodic window. The five periodic points in Fig. 12(g) represent synchronized flow on a torus for $\psi = 0.1130\pi$. The first period doubling of this solution is shown in Fig. 12(h).

The route to chaos which begins with a Hopf bifurcation and synchronization is not unusual. The Curry-Yorke model, for instance, synchronizes to three periodic points following a Hopf bifurcation.[13] The subsequent destabilization of flow on the torus similarly leads to chaotic behavior.

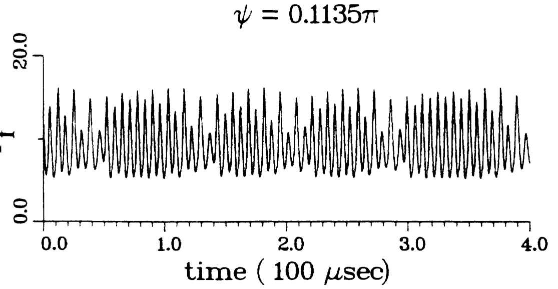

FIG. 14. Total fundamental intensity output (in arbitrary units) for $\psi = 0.1135\pi$.

## V. CONCLUSION

Our study of the nonlinear dynamics in intracavity doubled lasers began with a review of the rate equations used by Baer.[2] With the model restricted to three oscillating modes, our investigation of intensity output as a function of the cross saturation parameter revealed a type-III intermittency route to chaos. We extended the analysis of Oka and Kubota[6] to modify these equations to include the effect of a quarter wave plate in the cavity at an arbitrary angular setting. We found that the intensity output was stabilized when the KTP birefringence $\delta$ was an odd multiple of $\pi/2$, independent of the QWP angle.

We then studied the system behavior as the QWP angle was varied. The result was a route to chaos via Hopf bifurcation, synchronization, and period doubling. The presence of a periodic window was also observed.

We believe that Eqs. (2.13) require refinement to model all the important experimental features of intracavity doubling. A realistic model should explicitly identify the polarization directions of individual modes and account for the couplings between modes in the same polarization state, as well as between orthogonally polarized modes. We will present experimental results and a more complete theoretical treatment in a future publication.

## ACKNOWLEDGMENTS

G. J. acknowledges the sponsorship of the Air Force Institute of Technology and the U.S. Air Force Academy, Department of Mathematical Sciences. E. H. was supported by National Science Foundation (NSF) Grant No. DMS-8801309. The work of R. R. was supported by NSF Grant No. ECS-8722216 and by Mr. G. Bachman. We thank Tom Baer and Greg Kintz for useful discussions of intracavity doubled YAG lasers, and Jack Hale for helpful discussions of the model equations and references on homotopic continuation.

---

[1] R. L. Byer, Science **239**, 742 (1988).

[2] T. Baer, J. Opt. Soc. Am. B **3**, 1175 (1986).

[3] C. J. Kennedy and J. D. Barry, IEEE J. Quantum Electron. **QE-10**, 596 (1974).

[4] X.-G. Wu and P. Mandel, J. Opt. Soc. Am. B **4**, 1870 (1987).

[5] P. Mandel and X.-G. Wu, J. Opt. Soc. Am. B **3**, 940 (1986).

[6] M. Oka and S. Kubota, Opt. Lett. **13**, 805 (1988).

[7] See G. E. James, E. M. Harrell II, and R. Roy, in *Coherence and Quantum Optics IV*, edited by J. H. Eberly, L. Mandel, and E. Wolf (Plenum, New York, in press).

[8] F. T. Arecchi, in *Instabilities and Chaos in Quantum Optics* (Springer-Verlag, Berlin, 1987).

[9] H. Ito, H. Naito, and H. Inaba, J. Appl. Phys. **46**, 3992 (1975).

[10] J. K. Hale and N. Sternberg, J. Comput. Phys. **77**, 221 (1988).

[11] H. B. Keller, in *Applications of Bifurcation Theory*, edited by P. H. Rabinowitz (Academic, New York, 1977).

[12] Y. Pomeau and P. Manneville, Commun. Math. Phys. **74**, 189 (1980).

[13] P. Berge, Y. Pomeau, and C. Vidal, *Order Within Chaos* (Wiley, New York, 1984).

[14] S.-N. Chow and J. K. Hale, *Methods of Bifurcation Theory* (Springer-Verlag, Berlin, 1982), pp. 378–388.

[15] H.-O. Peitgen, in *Order and Chaos*, edited by H. Haken (Springer-Verlag, Berlin, 1982).

[16] M.-L. Shih, P. W. Milonni, and J. R. Ackerhalt, J. Opt. Soc. Am. B **2**, 130 (1985).

[17] T. Y. Fan, C. E. Huang, B. Q. Hu, R. C. Eckardt, Y. X. Fan, R. L. Byer, and R. S. Feigelson, Appl. Opt. **26**, 2390 (1987).